AIAA JOURNAL
Vol. 49, No. 7, July 2011

Fundamental Study of Modulated Transverse Jets from a Film-Cooling Perspective

Guillaume Bidan* and Dimitris E. Nikitopoulos†
Louisiana State University, Baton Rouge, Louisiana 70803

DOI: 10.2514/1.J050903

The effects of jet flow pulsation on a vertical jet in crossflow over a flat plate were investigated using Mie scattering visualizations, hot-wire anemometry, and large eddy simulations. An unforced-jet study was conducted over a wide range of blowing ratios to provide a baseline comparison with pulsed results and exhibited two distinct transverse jet regimes with characteristic vortical-structure dynamics, separated by a transitional region responsible for a significant drop in film-cooling performance. The influence of the forcing parameters such as blowing ratio, forcing frequency, and duty cycle on pulsed jets was investigated in terms of the vortical structures generated during the transient parts of the forcing cycle, as well as their impact on wall coverage and adiabatic effectiveness. Although jet forcing led to a global decrease in film-cooling performance when compared with relevant unforced results in most cases, instantaneous quantifications revealed improvements associated with the jet-pulse onset that, if correctly exploited by proper alteration of the forcing signal, could lead to overall improved pulsed-jet film-cooling metrics.

Nomenclature

BR	=	blowing ratio ($\rho_j W_j/\rho_\infty U_\infty = W_j/U_\infty$)
BR_h	=	high blowing ratio
BR_l	=	low blowing ratio
BR_m	=	mean blowing ratio
BR_{pp}	=	peak-to-peak blowing ratio ($BR_h - BR_l$)
C_c	=	coverage coefficient $C_c(\eta_x) = 1/A_j \int_{\eta \geq \eta_x} dA_{wall}$
D_j	=	jet diameter, mm
f_f	=	forcing frequency, Hz
H	=	boundary-layer shape factor (δ^*/θ)
L	=	jet pipe length, mm
Re_j	=	jet Reynolds number ($W_j D_j/\nu$)
Re_δ	=	boundary-layer Reynolds number ($U_\infty \delta/\nu$)
SR_h	=	stroke ratio ($BR_h U_\infty DC/f_f D_j = BR_h DC/St_\infty$)
St_j	=	jet Strouhal number ($f_f D_j/W_j$)
St_∞	=	freestream Strouhal number ($f_f D_j/U_\infty$)
t^*	=	normalized time after valve opening (tf_f), %
U_∞	=	average freestream velocity, $m \cdot s^{-1}$
W_j	=	average jet velocity, $m \cdot s^{-1}$
X_j	=	normalized streamwise coordinate (x/D_j)
Y_j	=	normalized spanwise coordinate (y/D_j)
Z_j	=	normalized vertical coordinate (z/D_j)
δ	=	99% boundary-layer thickness, mm
δ^*	=	boundary-layer displacement thickness, mm
η	=	adiabatic effectiveness ($(T_{wall} - T_\infty)/(T_j - T_\infty)$)
θ	=	boundary-layer momentum thickness, mm
ν	=	air kinematic viscosity, $m^2 \cdot s^{-1}$
ρ	=	air density, $kg \cdot m^{-3}$

Subscripts

area	=	area-averaged quantity
span	=	spanwise-averaged quantity

Received 3 September 2010; revision received 16 March 2011; accepted for publication 20 March 2011.

*Ph.D. Student, Department of Mechanical Engineering, Patrick F. Taylor Hall; gbidan3@lsu.edu. Student Member AIAA.

†Professor, Department of Mechanical Engineering, Patrick F. Taylor Hall. Member AIAA.

I. Introduction

FOR more than 50 years, cooling techniques (in particular, film cooling) have been successfully implemented to reduce thermal stress and allow operating turbine inlet temperatures to go several hundreds of degrees beyond materials limitations. Film-cooling systems involve arrays of small-diameter jets steadily injecting cool air at the surface of the part, thus protecting it from the hot crossflow gases. Individually, each jet in crossflow generates a set of characteristic vortical structures affecting the surface temperature, among which the most significant are the the shear-layer vortices, the counter-rotating vortex pair (CRVP), the wake vortices, and the horseshoe vortex (as described in [1]).

Numerous studies (such as [2,3]) have addressed passive geometrical optimizations such as jet compound-angle injection, exit shaping. and tab implementations, leading to adiabatic effectiveness values up to three times higher than the corresponding cylindrical geometries. Such improvements were essentially attributed to the weakening of the dominant mixing structures like the CRVP, film-separation avoidance, and increased jet spread by modification of the jet-exit velocity profile.

In addition, crossflow velocity unsteadiness existing beyond the first nozzle guide vanes has been shown [4,5] to drastically affect film-cooling performance through perturbation of the incoming boundary layer and passive jet flow pulsation.

An actively controlled film-cooling system using pulsed jets could provide adaptable jet-exit conditions while counterbalancing the undesirable effects of unsteady crossflow conditions found after the first nozzle-guide-vane stage.

Forced jets in crossflow using acoustic excitation or full modulation of the jet have been mostly studied in terms of mixing enhancement for fuel injection systems. Studies [6,7] have shown that penetration, mixing, and spread can be substantially increased by modulating the jet within a certain range of forcing frequencies. Although penetration and mixing should effectively be minimized for film-cooling purposes, increased lateral spread is highly desirable for improved coverage. Heat transfer measurements were conducted [8–10] on film-cooling systems involving fully modulated inclined jets using flow/no-flow types of pulsation. While results from [8] showed an overall decrease in performance when using forced jets, they seem to be in contradiction with results from [9,10], showing forced jets with higher effectiveness and somewhat lower heat transfer coefficients than comparable unforced results at equivalent mean blowing ratios. More recently, the effects of jet forcing in unsteady crossflow conditions created by a wake generator have been studied [11], and the conclusion was that forced jets did not provide improved metrics over steady jets under the conditions studied.

In view of the inconsistency of those results, the current study was oriented toward a more fundamental observation of the vortical structures associated with low-blowing-ratio forced jets in crossflow in order to gain insights into the reasons for such disparities. A series of experiments involving a fully modulated vertical jet in crossflow with variable low and high blowing ratios has been performed and compared with baseline unforced results. Although the 90 deg injection angle is recognized as a rather unfavorable configuration for film cooling, this geometry was selected as a classical and well-documented flow to investigate the effects of jet flow pulsation at low blowing ratios. It is worth pointing out that a past study [12] has shown that vertical jets in crossflow can perform better than streamwise inclined jets, albeit when used with short holes and narrow counterflow plenums. In [13] this improvement is attributed to the generation of in-hole vortical structures of opposite vorticity to that of the CRVP, thus weakening them and reducing crossflow entrainment and jet liftoff. It is believed that forcing the jet could lead to similar CRVP disruption effects, while promoting coolant spread at the wall, therefore providing improved film-cooling performance. This is part of the motivation of the study presented herein, which includes single-sensor hot-wire anemometry measurements and Mie scattering visualizations complemented by large eddy simulations to provide details on the flow and temperature field in the jet vicinity for both unforced and forced jets.

II. Experimental Apparatus and Methods

Experiments were conducted in an open-loop wind tunnel, the schematic of which is presented in Fig. 1, with a 3-m-long test section and a 0.9×0.6 m cross section. Optical access was available through a pair of transparent acrylic walls constituting the top and one of the side walls of the test section, respectively, allowing visualizations in planes parallel to the bottom wall (x-y) and along the jet symmetry plane (x-z). The coordinates x, y, and z are, respectively, associated with the streamwise, spanwise, and vertical directions of the flow, as shown in Fig. 1, and X_j, Y_j, and Z_j correspond to the normalized coordinates x/D_j, y/D_j, and z/D_j. The flow in the test section was laminar, with freestream turbulence intensity less than 0.5% and a constant freestream velocity U_∞ of 1.6 $\mathrm{m \cdot s^{-1}}$. The incoming crossflow boundary-layer characteristics were measured using hot-wire anemometry and are summarized in Table 1. The crossflow velocity profile and characteristics were kept constant throughout the study to limit the number of parameters affecting the flow behavior, focusing only on effects of jet bulk-flow modulation.

The jet exited from a round pipe with a diameter D_j of 25.4 mm located 762 mm downstream of the test-section inlet, mounted flush to the bottom wall. The air supply for the jet was regulated at 1.4 bar and dried using an inline desiccant dryer. At the jet inlet, the setup was composed of two branches, a principal and a bypass, each equipped with a metering needle valve controlling the flow in the branch. The bypass also included a computer-controlled solenoid valve used to pulse the flow during forced-jet experiments. This system gave the ability to independently set low and high flow rates in forced experiments, which were recorded by an inline flowmeter in a time-resolved manner at a sampling frequency of 1 kHz. An in-house seeding system injected water and titanium tetrachloride

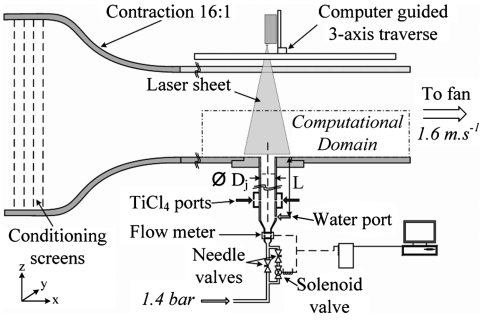

Fig. 1 Experimental setup schematic.

Table 1 Inlet boundary-layer characteristics at $X_j = -6$ and $Y_j = 0$

Parameters	Values
U_∞	1.6
Turbulence intensity	<0.5%
δ/D_j	0.630
δ^*/D_j	0.172
θ/D_j	0.077
H	2.23
$Re_\delta = U_\infty \delta/\nu$	1710

($TiCl_4$) vapors in two locations inside the jet to instantaneously generate titanium dioxide (TiO_2) particles used as tracer for Mie scattering visualizations. The flow driving the seeder was monitored and metered before the element introducing the $TiCl_4$ and accounted for in the calculation of the effective blowing ratio. The impact of seeding on the overall jet density was estimated to be less than 0.2% at the lowest blowing ratio of 0.15. The experiments were isothermal at room temperature, and the maximum temperature difference between jet and crossflow did not exceed 2°C, corresponding to a density-ratio variation less than 1%.

The tube length-to-diameter ratio effects have been substantially studied ([14–16], among others), showing that longer feeding tubes usually lead to better performance by decoupling the blade internal channel flow from the external one, thus preventing the jetting of the coolant. In addition, for $L/D_j > 7$, cooling performance was usually constant [16]. Therefore, in the current study, a value of $L/D_j = 12$ was chosen to allow for flow development, homogeneous seed mixing, and reduction of perturbations introduced by the seeding system.

Laser-sheet Mie scattering visualizations (both fully reacted and reactive), hot-wire anemometry, and time-resolved flow-rate measurement were used in this study and handled through analog/digital converters for synchronized acquisition and actuation. Since the density ratio was maintained at 1 in the current study, the blowing ratio, usually defined as the jet-to-crossflow mass-flux ratio, could be reduced to the jet-to-crossflow velocity ratio. Hot-wire anemometry measurements used for spectral characterization were performed at a sampling frequency of 5 kHz with appropriate Nyquist filtering at 2.5 kHz, using a single-wire probe (TSI model 1212-T1.5) with a sensing length of 1.27 mm ($D_j/20$). For mean flow and fluctuation intensities, the sampling time was sufficiently long to ensure no less than 5% uncertainty of the computed averages, whereas the sampling interval was longer than the local autocorrelation (integral) time scale to ensure statistically independent averages. Wavelet analysis was performed on high-sampling-frequency records to provide better insight into deterministic signatures observed under unsteady flow conditions, often masked when conducting Fourier spectrum analysis. This particular type of analysis was performed between 0 and 50 Hz using a modified version of an algorithm [17] with a Morlet wavelet of parameter 6, which was found to give satisfactory spectral and temporal resolutions.

Unforced-jet visualizations included a series of 96 images at each given blowing ratio and for each visualization plane. In averaged images (Fig. 4) using this sampling, the statistical uncertainty on individual-pixel grayscale intensity did not exceed 16%, and the area-averaged intensity uncertainty was less than 3%. The contrast-limited adaptive histogram equalization algorithm from MATLAB was applied to locally accentuate features in the images. The experiment was designed so that the jet natural frequencies were low (less than 100 Hz), and forcing was applied at frequencies lower than these natural frequencies while being consistently scaled down with respect to the experiments of [9] and in keeping with theoretical assessments of [18].

III. Numerical Setup

Numerical simulations were carried out in parallel to the experiments to provide additional information on the vortical structures

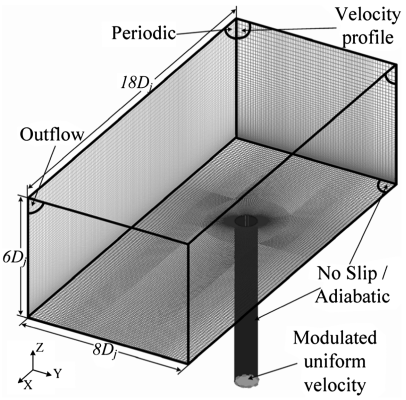

Fig. 2 LES domain and applied boundary conditions.

formed under unforced and forced conditions. FLUENT was used to simulate the unsteady turbulent flow through an incompressible large eddy simulation (LES) model using a dynamic Smagorinsky subgrid-scale model. Figure 2 shows the simulated domain and boundary conditions consisting of a rectangular box representing a part of the wind-tunnel test section used in the experiments and part of the jet feeding tube, also represented in Fig. 1.

The main computational domain was $18D_j$ long (x direction), $8D_j$ wide (y direction), and $6D_j$ tall (z direction), with $174 \times 92 \times 76$ cells along the respective dimensions. The pipe feeding the jet was $8D_j$ long, and the jet-exit center was located $6D_j$ downstream from the crossflow inlet. The jet pipe consisted of an O-grid mesh type with 3060 cells in the cross section and 150 cells along the pipe axis. This rather long section of the jet pipe was simulated (more than 450,000 cells) to allow flow development and prevent significant interference of the boundary conditions with the natural flow induced in forced experiments, which will be described in the following sections. The overall mesh was structured and comported 2 million cells. The first cells in contact with solid wall were $0.03D_j$ tall in the normal direction, yielding y^+ values close to unity. The simulation process started with Reynolds-averaged Navier–Stokes simulation to initialize the flow domain and obtain maximum viscous dissipation-rate ε estimates in the domain. The velocity and temperature fields were used to initialize the LES, and the viscous dissipation rate was used to compute the time step used in LES, which was less than the smallest Kolmogorov time scale ($\tau_R = \sqrt{v/\varepsilon}$). Thus, in the current simulations, the time step varied from 5×10^{-4} s at BR $= 0.15$ to 5×10^{-5} s at BR $= 4.3$. To obtain statistically significant data, several thousands of iterations were performed for each case on high-performance computing platforms using an average of 24 processors per run (IBM Power5+ at 1.9 GHz).

Velocity characteristics and boundary-layer profiles for the crossflow inlet of the computational domain were obtained from hot-wire measurements performed with the experimental setup (Table 1). Although extremely low (less than 0.5%), a divergence-free velocity perturbation component was superposed on the velocity profile using the spectral synthesizer method from FLUENT. At the inlet of the jet pipe, a uniform velocity was set to equal the experimental volumetric flow rate acquired with the flowmeter. In the forced-jet simulations, the jet inlet velocity was modulated in time by using the signal of the experimental unsteady volumetric flow-rate measurement. Similar to the crossflow inlet condition, a divergence-free perturbation component with a corresponding turbulence intensity of 30% was added to the velocity. These were estimated empirically from hot-wire measurements at the jet exit, since reaching a corresponding location inside the jet pipe was physically impossible. The jet and crossflow fluids in the simulation were maintained at constant temperatures of, respectively, $T_j = 300$ and $T_\infty = 330$ K, based on the experiments of [9], which did not affect the incompressible velocity field. These prescribed temperatures are also those used in the computation of the adiabatic effectiveness η.

Figure 3 presents a comparison between experimental and numerical velocity magnitude profiles taken at two distinct

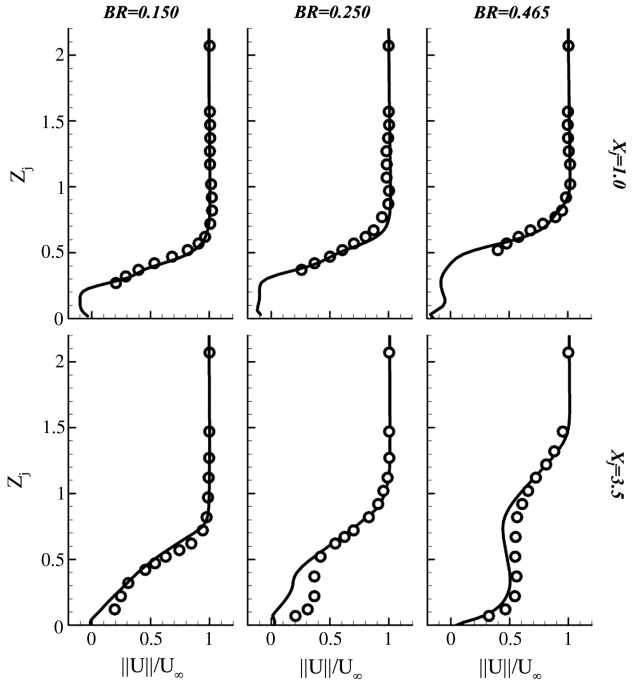

Fig. 3 Experimental (symbols) and numerical (solid line) velocity magnitude vertical profiles for $X_j = 1$ (top) and $X_j = 3.5$ (bottom), at BR $= 0.15$ (left), BR $= 0.25$ (middle), and BR $= 0.465$ (right).

streamwise locations at three unforced-jet blowing ratios. Experimental data were acquired using a single-component hot-wire probe in the plane $Y_j = 0$ and purely for providing some confidence that the numerical results obtained with the imposed inlet conditions (especially for the jet) were reasonable. With the single-wire probe used, the measurements did not provide a distinction between streamwise and vertical components of the velocity; thus, the comparison was made on the velocity magnitudes $\|U\|$. In addition, recirculatory flow present near the wall at $X_j = 1.0$ could not be resolved using this type of probe; therefore, no data are provided in such areas. The velocity profiles in Fig. 3 compare reasonably well at BR $= 0.15$ and 0.465 for both streamwise locations, whereas at BR $= 0.25$, the simulations appear to underpredict the velocity magnitude in the jet wake. This result is consistent with a mismatch in the transition behavior between experimental and numerical data, which will be described later. Overall, the agreement of the rudimentary mean flow comparisons between simulation and experimental results is quite good and reenforces the qualitative comparisons from visualizations presented in the following sections. Thus, both physical and simulated flows appeared comparable enough to be used concurrently in interpreting and understanding fundamental processes.

IV. Unforced Jet

A. Experimental Results

Unforced jets were investigated over a wide range of blowing ratios from BR $= 0.15$ to 4.3, respectively, corresponding to Re_j values of 410 to 11,600, to be put in perspective with the relatively low value of Re_∞ mentioned previously. Based on the characteristic vortical structures, two distinct jet regimes for BR < 0.275 and BR > 0.6 were identified. A transition regime was found at intermediate values of the blowing ratio, exhibiting vortical structures that are typical of both regimes.

Figure 4a shows visualizations corresponding to the low-blowing-ratio attached regime. Though of particular interest for film cooling, only a few studies oriented toward vortical-structure characterization have dealt with such low blowing ratios. Among them, the presence of a recirculation region directly downstream of the jet exit has been described [19], which was also found in the present study of reactive Mie scattering visualizations. A horseshoe vortex is located partly

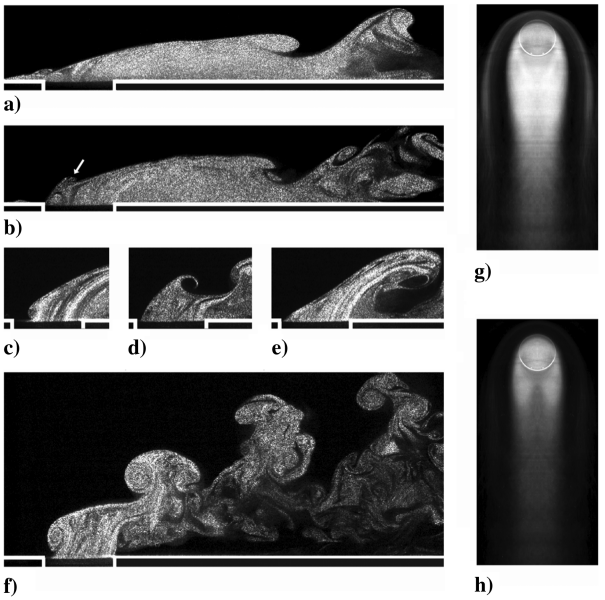

Fig. 4 *X-Z* plane Mie scattering visualizations (left) and time-averaged *X-Y* visualizations at $Z_j = 0.125$ (right) at a) BR = 0.188, b) BR = 0.25, c–e) BR = 0.365, f) BR = 0.6, g) BR = 0.365, and h) BR = 0.465.

above the jet exit and is essentially identical to that described in [1,20]. Shear-layer vortices are formed in the lower jet shear layer as the result of Kelvin–Helmholtz type of instability, consisting of interlocked hairpin vortices, similar in nature to those described in [21] for coflowing jets. As these structures are convected downstream, the "legs" of the hairpins move toward the symmetry plane ($Y_j = 0$) and away from the wall, while their "heads" progressively penetrate in the crossflow. In Fig. 4a a stable rollup appears to take place inside the jet tube on the windward edge, prevented from shedding by the advanced position of the horseshoe vortex. This structure was also observed in [22] with an extremely low blowing ratio of 0.1, where it occupied half the jet exit. The outer structures in Fig. 5a indicated by arrows A and C are systematically present in the attached jet configuration. Initially in the streamwise direction, these vortices are reoriented in the spanwise direction further downstream in the vicinity of hairpin vortices to form *X*-patterned structures. Arrow B in Fig. 5a shows another type of vortical structure formed at low blowing ratios, corresponding to an inverted hairpin vortex. Further details on the dynamics and evolution of the characteristic vortical structures will be examined later, aided by simulation results. For $0.225 \leq \mathrm{BR} < 0.275$ the jet dynamics are, in essence, identical

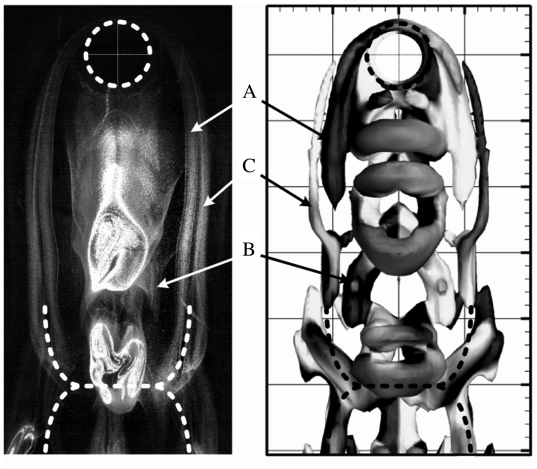

Fig. 5 Instantaneous *X-Y* view at BR = 0.188 from a) Mie scattering visualizations and b) LES $\Delta P = 3000$ isosurface shaded by spanwise vorticity (negative is black and positive is white).

to those described at a lower BR, with the exception of successive horseshoe-vortex transports over the top of the jet/crossflow upper interface, as evidenced in Fig. 4b. This destabilization is likely provoked by the higher position of the inner vortex observed in Fig. 4b, where it is partially outside the jet pipe. Once detached, the horseshoe vortex is convected downstream, eventually merging with shear-layer vortices of identical positive *Y* vorticity. It has been observed that this shedding usually occurs sequentially, followed by periods of stability.

The case BR = 0.275 marks the actual transition from the attached regime to the detached one with successive detachments of the inner vortex shown in Figs. 4c–4e. After the convection of this structure, ingestion of crossflow fluid inside the jet pipe occurs at the leading edge in Fig. 4c and is followed by the transport of the horseshoe vortex in Fig. 4d. The crossflow ingestion has the effect of a partial blockage of the jet-exit area, locally increasing the blowing ratio and triggering the formation of a large hairpin vortex in Fig. 4e. The transported inner vortex, which is relatively small in Fig. 4c at BR = 0.365, becomes comparable in size with the downstream shear-layer vortices as BR approaches 0.6. Because of the increasing jet strength, the extent of the crossflow ingestion after the inner vortex transport gradually decreases until disappearing at BR = 0.6. The combination of the transported inner vortex and the lower shear-layer vortices constitute the well-known shear-layer vortices observed in higher-blowing-ratio configurations. In the rest of this paper, this intermediate jet configuration between attached and detached jet regimes will be called transitional, although it is not related to the usual transition from laminar to turbulent flow. Similarly, the lower-blowing-ratio boundary of this regime (BR = 0.275) will be referred to as the transition threshold.

Cases with BR > 0.600 (corresponding to Reynolds number above 1650), exhibit a completely detached jet, comparable with that observed in [1,20]. The shear-layer ring vortices are formed periodically and appear in Fig. 4f as well-defined rollups on both the upper and lower jet/crossflow interfaces, deeply penetrating in the crossflow as they are convected away from the jet exit. The wake vortices observed under the jet appear to transport tracer particles, hence providing marginal coverage downstream of the jet exit.

Single-component hot-wire measurements performed at the jet exit and in the upper shear layer (both above the jet exit and at a downstream location of $X_j = 3.5$) were analyzed using wavelet spectral analysis to identify fundamental modes, which are summarized in Fig. 6. Measurements performed at the jet exit and above did not reveal characteristic frequencies for BR ≤ 0.225, since at such low blowing ratios, the velocity fluctuations due to the shear-layer instability were relatively weak near the jet exit (see Fig. 4a). At

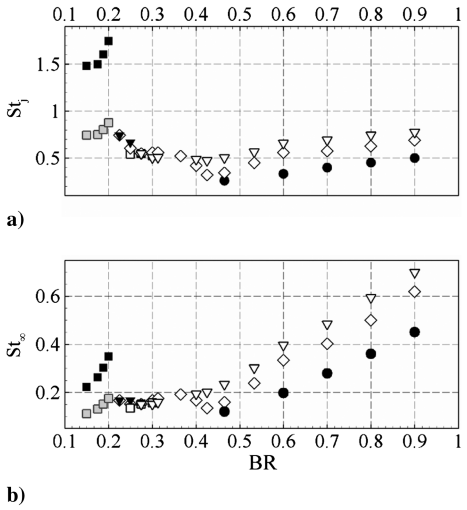

Fig. 6 Fundamental frequencies from hot-wire anemometry at ◇ $X_j = 0$, $Z_j = 0$; ▼ $X_j = 0$, $Z_j = 0.25$; ▽ $X_j = 0$, $Z_j = 0.5$; ■ $X_j = 3.5$, $Z_j = 0.75$ (gray squares are the corresponding first subharmonic); □ $X_j = 3.5$, $Z_j = 1.0$; from LES ● $X_j = 0$ $Z_j = 0$.

the downstream location, results show increasing fundamental Strouhal numbers with respect to the blowing ratio, characterizing the rate of formation of hairpin vortices. Similarly, results corresponding to the detached regime (BR > 0.6) show a linear growth rate of the ring vortices' formation frequency with respect to the blowing ratio at both locations. The linear increase in Strouhal number for the detached jet is in agreement with previous results from [23] for $1 < \mathrm{BR} < 3.5$ and is explained by a decrease in the jet shear-layer thickness as the blowing ratio is increased, evolving from a weak jet to a stronger jet with an associated increase in the characteristic Strouhal number of the jet column mode. In [23] the linear rate at which the Strouhal number varied with respect to the blowing ratio was approximately $1/5$. In the present study, it was found to be 2/5 for the range $0.465 \leq \mathrm{BR} \leq 0.9$. This difference can be attributed to numerous factors, such as the operating Reynolds number, the crossflow boundary-layer thickness, and, especially, the jet velocity exit profile. It should be noted that fundamental frequencies obtained for the attached jet appear to be significantly higher than equivalent signatures obtained at higher blowing ratios. This is explained by the fact that data for the first regime were obtained mostly at $X_j = 3.5$ near the wall, where measurements were influenced by the passage of inverted hairpin vortices formed in-between the primary hairpin vortices (see Fig. 5b), hence doubling the passage frequency of the primary structures, since the hot-wire probe does not discriminate between the different vortices. To provide a more relevant comparison base, the corresponding subharmonics for those measurements are provided in Fig. 6 (gray squares) and show better agreement with characteristic frequencies at higher blowing ratios. The usefulness of the wavelet analysis in unforced conditions was found in the transition regime, where series of events were more transient in nature (e.g., intermittent horseshoe-vortex transports), thus making the identification of characteristic frequencies difficult with Fourier spectrum analysis. For $0.225 < \mathrm{BR} < 0.35$, the fundamental signatures seem relatively constant around $St_\infty = 0.15$, even above $\mathrm{BR} = 0.275$, where the inner vortex starts to be convected. The inner vortex is most likely convected as a result of the perturbation created by the horseshoe-vortex transport, the frequency of which is better scaled by the crossflow velocity, as evidenced by Fig. 6b for $0.225 \leq \mathrm{BR} < 0.275$. When BR is increased, the natural shedding of the inner vortex observed in the transitional cases becomes predominant over the transport of the horseshoe vortex and a decrease in fundamental frequency is observed for $0.35 \leq \mathrm{BR} < 0.6$ at the jet exit before growing again as the detached regime settles in.

B. Numerical Results

For the LES results, the Laplacian of the pressure (ΔP) was computed and isosurface rendering was used to represent the vortical structures, based on the work in [24] for incompressible flows. The simulations at $\mathrm{BR} = 0.188$, illustrated in Fig. 5, together with an experimental visualization counterpart, show good qualitative agreement with the experiment and exhibit identical structures. Numerically resolved structures include the horseshoe vortex (marked A), inverted hairpin vortices (marked B), and a pair of counter-rotating streamwise vortices located outside of the horseshoe vortex (marked C). Inverted hairpin vortices are formed in the wake of the hairpin vortices as both upper and lower shear layers merge together, therefore yielding strong velocity gradients between the crossflow and recirculation regions, which leads to the formation of an additional vortex. As they are convected, the inverted hairpins stay close to the wall, due to their mutual induction with regular hairpin structures. The origins of the near-wall secondary structures (Fig. 5 arrow C) are explained by the presence of a high-pressure region (P^+) located directly above the jet, as shown in Fig. 7, resulting in an adverse pressure gradient for part of the jet fluid. A stable rollup is then formed inside the jet pipe at the upstream edge (arrow C), which corresponds to the inner vortex only partially visible in the experimental visualizations of Fig. 4a. This vortex is connected to the legs of the hairpin vortices to form interlocked ring vortices of which only the downstream part is convected, as shown in the schematic of

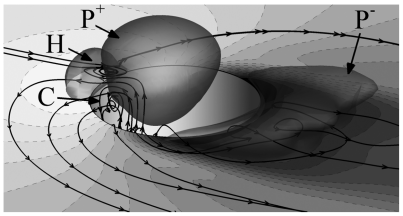

Fig. 7 Pressure regions at the jet exit at BR = 0.188, referenced by exit average pressure at $X_j = 0$, $Y_j = 0$, and $Z_j = 0$ from LES.

Fig. 8a. The presence of the high-pressure region above the jet forces part of the fluid to exit the pipe on the sides between the principal horseshoe vortex and the wall with nonzero spanwise velocity (see Fig. 7). This adds to the crossflow deflection induced by the jet blockage and creates a positive velocity gradient in the vertical direction, generating streamwise vorticity. Consequently, the fluid rolls up into a pair of counterhorseshoe vortices of opposite vorticity to the principal horseshoe vortex shown in Fig. 5b. Figures 5 and 8a also show that the horseshoe vortex is weakened near the legs of the hairpin vortices, due to their relatively stronger opposite vorticity, so that counterhorseshoe and horseshoe vortices are alternating in strength. The induction produced by their respective mirror images with respect to the bottom wall entrains the horseshoe vortex away from the symmetry plane ($Y_j = 0$) and entrains the counter-rotating horseshoe vortices toward it. At the same time, they are reoriented in the spanwise direction directly downstream of the shear-layer vortices' heads as they are subjected to their relatively stronger velocity field. The combination of horseshoe and counter horseshoe vortices results in the X-patterned structures previously observed in Fig. 5.

From a film-cooling perspective it is interesting to identify the vortical structures potentially influencing the wall temperature field.

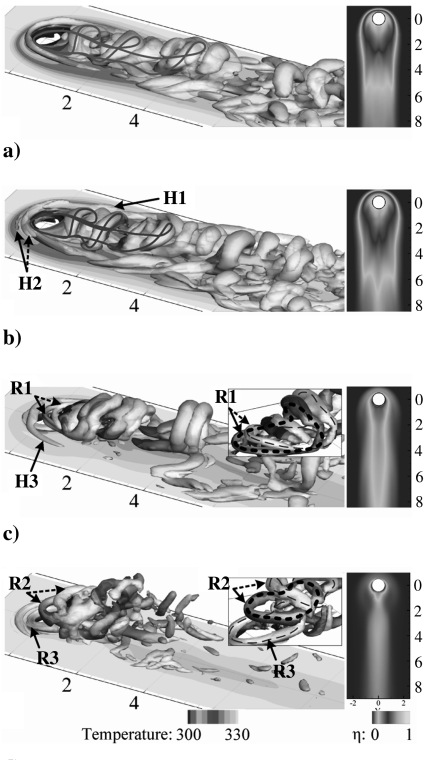

Fig. 8 ΔP isosurfaces at two superposed time instants separated by Δt (left) and corresponding time-averaged wall adiabatic effectiveness from LES: a) BR = 0.188, $\Delta P = 1500$, and $\Delta t = 20$ ms, b) BR = 0.25, $\Delta P = 2000$, and $\Delta t = 35$ ms, c) BR = 0.465, $\Delta P = 5000$, and $\Delta t = 10$ ms, and d) BR = 0.9, $\Delta P = 1500$, and $\Delta t = 10$ ms. The first isosurface is shaded by temperature.

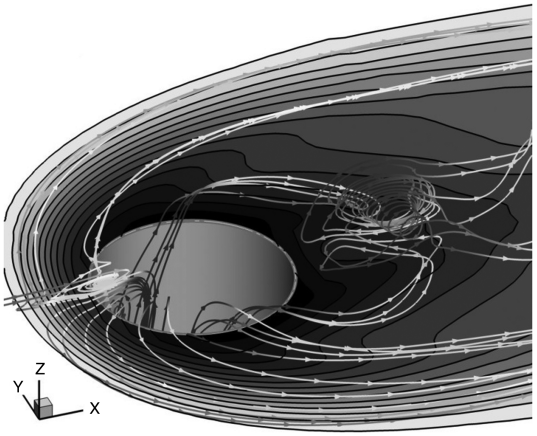

Fig. 9 Instantaneous streamlines and wall temperature contours from LES at BR = 0.188.

Figure 8a shows that the area of highest adiabatic effectiveness in the attached configuration is located in the recirculation region, which is essentially seeded by jet fluid. The fluid forced to exit on the sides of the jet pipe by the high-pressure region is also providing additional coverage, as shown in Fig. 9. This figure also shows the effect of the horseshoe vortex on wall adiabatic effectiveness as it entrains significant amounts of coolant upstream of the jet, due to its position above the jet exit. The counterhorseshoe and horseshoe vortices have an opposite impact on the jet spread at the wall because of their respective velocity fields. Indeed, near the wall the horseshoe vortex has a velocity field pointing away from the symmetry plane and tends to entrain cooler fluid from the jet core region toward the wall, whereas the counterhorseshoe vortices have an associated opposite velocity field carrying freestream fluid near the bottom surface. Consequently, the formation of the X-patterned structures directly downstream of the hairpin vortices results in a dramatic decrease in local wall adiabatic effectiveness. Along the symmetry plane, the legs of the hairpin vortices are responsible for the transport of most of the coolant. These results show the significant role of the horseshoe vortex and the inner vortex in the jet coverage near the wall.

As observed in the experiments for BR = 0.25, the horseshoe vortex is convected, while the inner vortex oscillates inside the jet pipe. After the transport of the horseshoe vortex is initiated (Fig. 8b, H1), a second one is instantaneously formed in the crossflow boundary layer (Fig. 8b, H2) so that the coolant supply upstream of the jet exit is never interrupted and coverage is continuously provided to this area. As BR increases, the horseshoe vortex is strengthened and pushed further upstream from the jet exit, thus augmenting the jet coverage at the wall. Finally, the hairpin vortices at BR = 0.25 are stronger when compared with the lower-blowing-ratio cases and stay coherent further downstream, carrying more coolant along the symmetry plane.

Figure 8c presents results corresponding to a transitional jet at BR = 0.465, showing the immediate liftoff of the hairpin vortices' legs after the jet exit because of increased mutual induction, as well as the shedding of the inner vortex. Each inner vortex is directly connected to a downstream rollup and forms a ring vortex, typical of higher-blowing-ratio regimes and shown in Fig. 8c as R1, that rapidly dissipates as it is convected in the freestream. After the inner vortex shedding, the adverse pressure gradient exerted by the jet on the crossflow boundary layer decreases and triggers the transport of the horseshoe vortex (Fig. 8c as H3). A burst of jet fluid due to partial crossflow ingestion results in the formation of a large hairpin vortex, and a second horseshoe vortex eventually reforms once the jet recovers from the ingestion and the jet/crossflow interface is stabilized. The drop in coverage observed in the experiments (between Figs. 4g and 4h) and the contours of adiabatic effectiveness in Fig. 8 is explained by the consecutive transports of the inner and horseshoe vortices interrupting the coolant flow upstream and on the sides of the jet. Hence, the transitional regime marks the beginning of coverage degradation occurring well before the detached regime settles in.

According to Fig. 8d, at BR = 0.9 the shear-layer ring vortices (R2) are formed on a periodic basis and are directly convected away from the wall, therefore not providing coverage. Conversely to the transitional regime, the horseshoe vortex formed ahead of the jet is not convected, though it oscillates as the shear-layer ring vortices are shed, and its influence on the wall temperature appears insignificant in Fig. 8d. Marginal amounts of coolant reach the jet-wake region transported by the wake vortices, as evidenced by the η contours of Fig. 8d, as well as the presence of seed particles in experimental Mie scattering visualizations of Fig. 4.

Figure 10a shows spanwise-averaged adiabatic effectiveness from the numerical results. As expected from the contour plots in Fig. 8, η_{span} increases with increasing values of the blowing ratio until the transitional threshold is reached and then drops precipitously. As BR continues to increase, the effectiveness decreases asymptotically toward zero. A local minimum in η_{span} profiles for the transitional/detached jet is observed downstream of the jet exit, corresponding to the location where the crossflow recovers behind the jet and tends to move upstream toward the jet exit as BR increases.

The area-averaged adiabatic effectiveness η_{area} presented in Fig. 10b was computed from the simulations, assessing the overall film-cooling performance at a given blowing ratio. According to η_{span}, film cooling is improved for increasing values of BR below the transitional threshold and decreases dramatically beyond this point. A coverage coefficient C_c was defined and computed from the simulations based on total wall area over which the adiabatic effectiveness maintains a value above a set threshold normalized by the jet-exit area. As opposed to the η_{area}, the coverage coefficient gives a global performance index in terms of covered area. Estimating performance based only on η_{area} does not distinguish a configuration with a localized high η peak from one with a lower peak, but greater and more homogeneous coverage. Figure 10b presents three trends of C_c for adiabatic effectiveness thresholds of 0.2, 0.3, and 0.5. From these results, all trends show a drastic drop of each metric beyond BR = 0.415, after an increase with BR up to this threshold for most. The combination of the reduction in both η_{area} and C_c shows that both the overall value of adiabatic effectiveness and the covered area are decreased. The coverage degradation is associated with the passage of the jet from the attached to the transitional regime and the disruption of coolant supply to the upstream and side regions resulting from the shedding of the inner vortex. Such a sharp coverage decrease was also observed in the experiments through estimated seed concentration profiles in a plane directly above and parallel to the wall (not presented in the current paper, for the sake of brevity). The abruptness of the performance degradations beyond the transitional blowing ratio suggests that operating the system near this point is highly hazardous, since a slight change in crossflow velocity could have dramatic consequences on cooling performance.

A discrepancy between experiments and simulations was observed in the value of the transitional blowing-ratio threshold, which was found to be at BR = 0.275 experimentally but at BR = 0.415 in LES. This quantitative discord was attributed to the sensitivity of the flow to the jet inlet conditions, which are not exactly matched between the experiment and the simulations and are

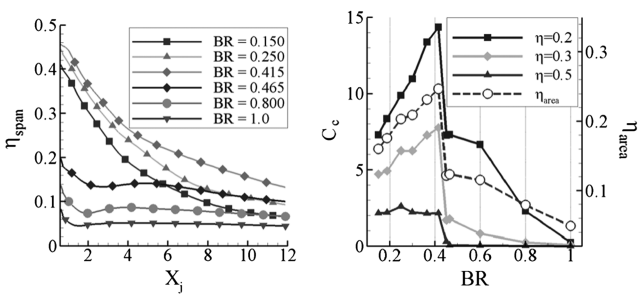

Fig. 10 Plots of a) spanwise-averaged adiabatic effectiveness and b) area-averaged adiabatic effectiveness and coverage coefficient for thresholds η = 0.2, 0.3, and 0.5 as a function of BR from LES.

particularly difficult to achieve both in terms of turbulence intensity, length scales, and velocity profile. This is partly so because of the presence of the seeding injection system and the difficulty of obtaining time-resolved velocity distributions in the jet supply tube during the experiments. For the same reasons the characteristic frequencies of the shear-layer structures were found to be somewhat lower in the numerical simulations (Fig. 6), though their rate of increase with respect to the blowing ratio agrees well with the experimental trends.

Investigations of the unforced jet have shown that the transitional threshold constitutes a limitation to the improvement of film-cooling performance because of the transport of the inner vortex and the associated interruption of coolant supply to the upstream region. Based on the evolution of the film-cooling metrics in the attached jet regime, delaying the transport of the inner vortex to higher values of BR could lead to improved overall coverage.

V. Forced Jet

A. Experimental Results

Forced-jet experiments were carried out using a nominal square wave excitation over a large range of forcing parameters; those presented in this paper are summarized in Table 2. Each case was observed at 4 forcing frequencies of 0.5, 1.0, 5.0, and 10.0 Hz, respectively, corresponding to Strouhal numbers of $St_\infty = 0.008$, 0.016, 0.079, and 0.159. These frequencies were selected to extend well below the shear-layer vortices' natural frequencies of the corresponding unforced flows to avoid resonant amplification, potentially leading to undesirable mixing enhancement (see [18]) and are consistent with previous studies on unsteady film cooling [9,11]. Forced-jet observations were carried out using Mie scattering visualizations and hot-wire anemometry (constant temperature anemometry) and the use of time-resolved flowmeter measurements allowed for precise knowledge of the forcing conditions.

The flow visualizations revealed vortical-structure characteristic of forced jets mostly initiated in the transient parts of the cycles (high-blowing-ratio onset, low-blowing-ratio dropoff). At the high-blowing-ratio onset a starting vortex is formed, due to the increased shear generated by the abrupt change in velocity. This is a well-known feature previously reported in many other forced-jet experiments, such as [7,25,26], although most of these studies have been carried out for mixing and penetration enhancement and generally involved both higher blowing ratios ($BR_m > 2$) and forcing frequencies ($St_\infty > 0.250$, except for [26]), compared with the present study. They exhibited starting vortices consisting of single vortex rings penetrating deeply in the crossflow, compared with the corresponding unforced jet.

Figure 11 presents the four types of starting structures encountered in the current study, depending on the forcing parameters. In Figs. 11a–11d, the sequence shows the formation of a leading vortex ring, followed by a trailing column, and in Fig. 11e the vortex ring is formed alone. In Fig. 11f a leading hairpin vortex is followed by a series of smaller shed hairpin vortices, and in Fig. 11g a single hairpin vortex is generated.

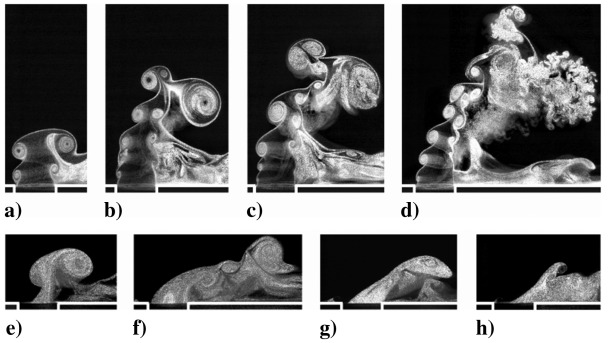

Fig. 11 *X-Z* Mie scattering visualizations for a)–d) case 22 $St_\infty = 0.008$, $t^* = 1, 3, 4, 6$ (from distinct cycles); e) case 8 $St_\infty = 0.159$, $t^* = 30$; f) case 9 $St_\infty = 0.079$, $t^* = 36$; g) case 5 $St_\infty = 0.159$, $t^* = 60$; h) case 16 $St_\infty = 0.079$, $t^* = 64$.

Table 2 Experimental forcing conditions

No.	BR_m	BR_l	BR_h	DC	No.	BR_m	BR_l	BR_h	DC
1	0.250	0.188	0.313	50	13	0.350	0.188	0.395	70
2	0.250	0.213	0.363	25	14	0.350	0.288	0.538	25
3	0.250	0.175	0.325	50	15	0.350	0.225	0.475	50
4	0.250	0.145	0.295	70	16	0.350	0.175	0.425	70
5	0.250	0.188	0.438	25	17[a]	0.450	0.188	0.712	50
6	0.250	0.125	0.375	50	18	0.450	0.188	0.562	70
7	0.250	0.075	0.325	70	19	0.450	0.388	0.638	25
8[a]	0.350	0.188	0.836	25	20	0.450	0.325	0.575	50
9[a]	0.350	0.188	0.513	50	21[b]	0.750	0.250	2.25	25
10	0.350	0.188	0.419	70	22[b]	0.750	0.250	1.25	25
11	0.350	0.313	0.463	25	23[b]	1.25	0.250	4.25	25
12	0.350	0.275	0.425	50	24[b]	1.25	0.250	2.25	50

[a]Simulations carried at these conditions.
[b]Flowmeter record unavailable.

These results show reasonable agreement with the previous experimental observation in [27] on strong fully modulated jets at $BR_h > 3$, evidencing three of the four regimes encountered here. The study in [27] also exhibits an additional turbulent regime for higher values of the stroke ratio (SR_h), not reached in the present work. Although a mapping of the various starting-vortex regimes is available in [27], the significantly stronger jets used in that study, along with the chosen set of parameters used in the mapping, oriented toward the study of starting-vortex interactions, prevents a direct quantitative comparison with the current study and, in particular, Fig. 12. Good agreement is also found with the LES results from [28], covering relatively low values of blowing ratios ($BR_h \geq 1$), although only three types of starting vortices were pointed out and sorted as a function of the stroke ratio and the blowing ratio. These parameters were chosen based on the work proposed in [29] on the existence of a limiting stroke ratio (formation number) beyond which a piston-induced vortex ring is shed due to circulation saturation. The same type of classification was adopted for the present study with a partly modulated jet using several parameter definitions, such as the stroke ratio based on BR_m, BR_{pp}, or BR_h. Since the duration of the low-blowing-ratio part of the cycle was not expected to influence the characteristics of the starting vortex, the scaling parameter BR_m was set aside. Of the two remaining possibilities, it was found that both BR_h/SR_h and BR_{pp}/SR_{pp} provided a similar classification, though BR_h versus SR_h gave better-defined zones and limiting values and was therefore adopted in Fig. 12. According to this figure, pulsed cases can be decomposed into two principal regimes with respect to the type of starting vortex generated at the jet onset: one corresponding to the formation of vortex rings ($BR_h > 0.584$) and the other corresponding to the formation of hairpin vortices ($BR_h < 0.584$). In the first regime, a subcategory is found at large enough stroke ratios, with the development of a trailing column composed of smaller ring vortices in the wake of the leading starting-vortex ring (Figs. 11a–11d). It has been observed in some limiting cases that the formation of a short trailing column composed of a single vortex would occur irregularly from one cycle to the other, which determines the critical stroke ratio for a given BR_h value. The results obtained in the present study show an excellent agreement with the numerical simulations in [28], although the limiting BR_h between hairpin- and ring-vortex formations was found to be $BR_h = 0.584$ in the current study, as opposed to $BR_h = 2$ in [28]. In addition, the current study also shows the presence of a subcategory in the starting-hairpin-vortex regime; at low values of SR_h, a single large hairpin vortex is formed (Fig. 11f), and at larger values of SR_h, series of weaker hairpin vortices follow the leading starting vortex (Fig. 11g). In essence, these hairpin vortices are very similar to those observed in unforced conditions, except for the considerably larger size of the leading one.

The dynamics of the starting vortices have been observed and show good agreement with the numerical results from [28]. When a single vortex ring is formed, the ring is convected downstream and

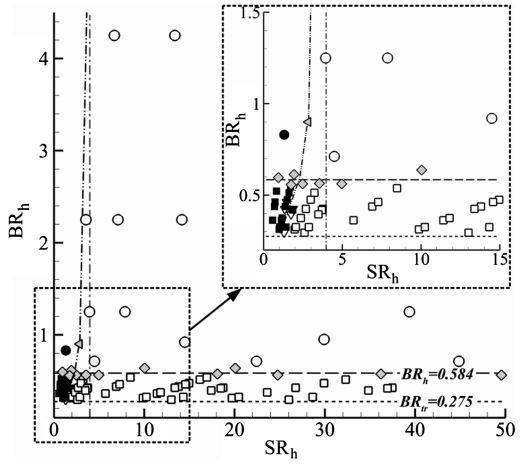

Fig. 12 Classification of the starting-vortex type with respect to SR_h and BR_h: \circ leading vortex ring and trailing column, ● single vortex ring, ◁ limiting-case vortex ring with/without trailing column, □ leading hairpin vortex and trailing hairpins, ■ single hairpin vortex, ◇ limiting-case hairpin/ring vortex, and ▽ limiting-case hairpin vortex with/without trailing vortices.

tilts negatively with respect to the y axis. The downstream rollup increases in size, while the upstream part is reduced, due to the shear exerted by the crossflow. When a trailing column is formed, the initial ring vortex tilts in the downstream direction, while the downstream rollups of the ring vortices forming the trailing column are convected upward more rapidly than their upstream counterparts, due to mutual induction and the difference in pressure between the windward (high-pressure) and leeward (low-pressure) sides. This is confirmed by the ingestion of the downstream part of the first trailing ring vortex by the leading vortex observed in several cases, as in Fig. 11b. This counterclockwise rotation is important to note, since it induces vertical vorticity from the side arms of the trailing-column vortices and provides a vorticity source for the initialization of the CRVP, the roots of which are observed in the background of Figs. 11c and 11d. It is highly unlikely the film-cooling metrics will benefit from the formation of ring vortices, as they carry considerable amounts of jet fluid away from the bottom wall and trigger the instantaneous transport of the inner vortex. Figure 12 shows that in cases corresponding to the lower right corner ($BR_h < 0.584$, large SR_h), hairpin starting vortices are formed at blowing ratios above the unforced transitional threshold of 0.275 for a certain amount of time after the jet onset, during which the inner vortex stays attached. This parametric window is one of potential improvement in terms of film-cooling performance.

At the transition from BR_h to BR_l, most of the cases with $BR_{pp} > 0.15$ exhibit ingestion of crossflow fluid at the upstream edge of the jet pipe, as shown in Figs. 11e and 11h. When ingestion occurs, the existing horseshoe vortex is destabilized by the displacement of the jet/crossflow interface and is convected downstream. The duration of the low part of the cycle (equal to $(1 - \mathrm{DC})/f_f$) determines whether the jet will recover from the ingestion or not. Therefore, given enough time, the structures observed in the low part of the cycle will eventually be identical to those observed for the unforced jet at corresponding blowing ratios. The absence of seeding in the crossflow, as well as the inability to observe the flow inside the jet pipe, prevented a detailed study of the impact of the transition from BR_h to BR_l on the jet vortical structures during the experiments.

Overall, cases at forcing frequency of $St_\infty = 0.008$ and 0.016 were such that the cycle was long enough to allow the transient regimes to wash out in both the high and low parts of the cycle and exhibited four distinct regimes per cycle: a transient regime from BR_l to BR_h with the formation of starting vortices, a quasi-unforced high-blowing-ratio state, a transient regime from BR_h to BR_l with crossflow ingestion inside the jet pipe, and a quasi-unforced low-blowing-ratio state. On the other hand, higher-forcing-frequency cases ($St_\infty =$ 0.079 and 0.160) only comported two transient regimes.

The time-dependent capabilities of the wavelet analysis were particularly useful in forced experiments, in which continuous

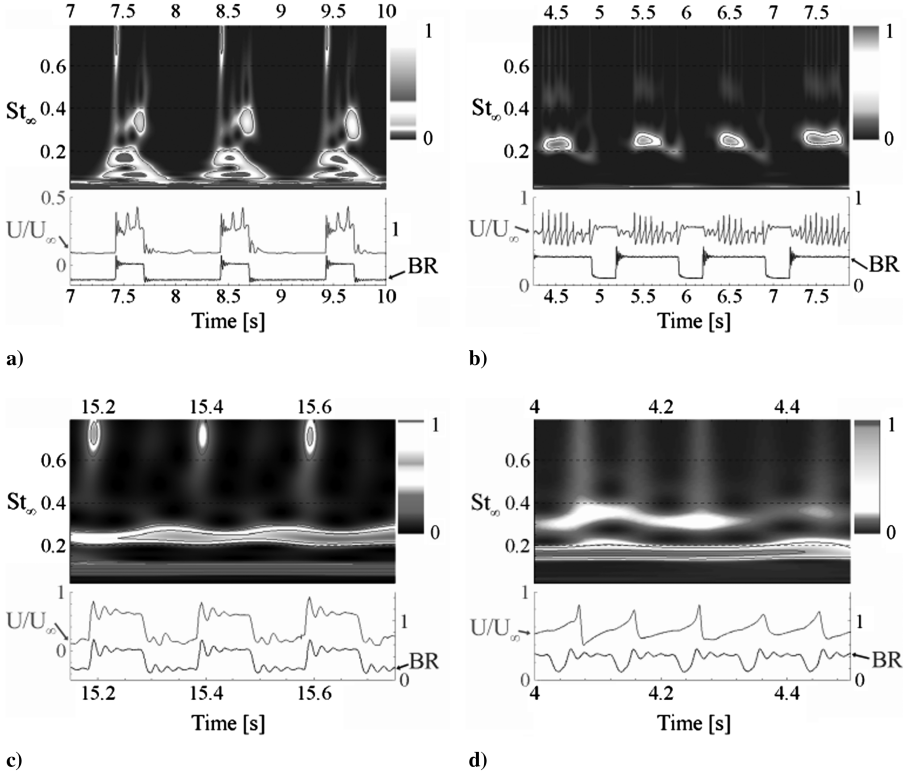

Fig. 13 Wavelet analysis performed on constant-temperature-anemometry records for $Y_j = 0$: a) at $X_j = 0$ and $Z_j = 0$ in case 5 for $St_\infty = 0.016$, b) at $X_j = 0$ and $Z_j = 0.5$ in case 7 for $St_\infty = 0.016$, c) at $X_j = 0$ and $Z_j = 0$ in case 9 for $St_\infty = 0.079$, and d) at $X_j = 0$ and $Z_j = 0.5$ in case 16 for $St_\infty = 0.159$. Wavelet normalized energy as a function of time and St_∞ (top row), along with analyzed instantaneous hot-wire measurement and corresponding instantaneous blowing ratio (bottom row).

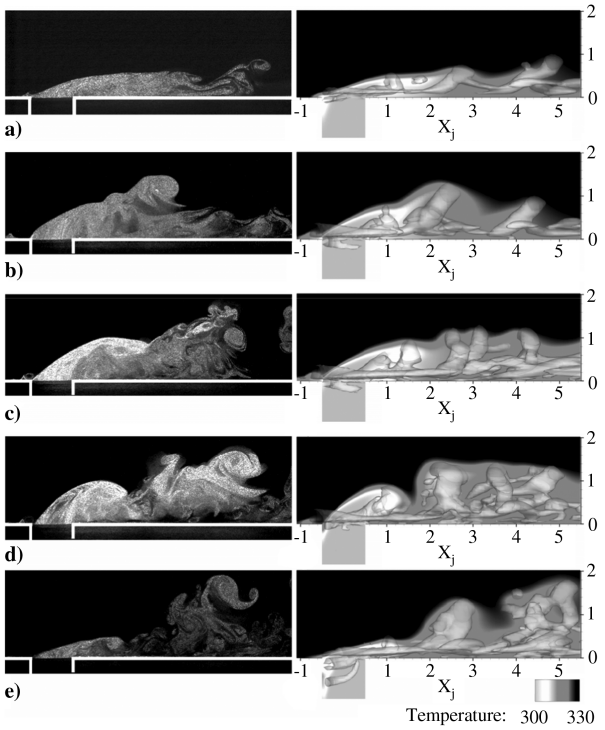

Fig. 14 ***X-Z*** **Mie scattering visualizations from** $\mathbf{BR}_m = 0.35$**, DC = 50% (case 9) at** $St_\infty = 0.016$ **(left column) and** ***X-Z*** **temperature slice from LES and** $\Delta P = 3000$ **isosurfaces at identical forcing conditions (right column). Time stamps correspond to Fig. 17; a)** $t^* = -3$**, b)** $t^* = 8$**, c)** $t^* = 20$**, d)** $t^* = 43$**, and e)** $t^* = 60$**.**

transitions between several regimes involving different characteristic frequencies were encountered throughout a single cycle. Figure 13 shows constant-temperature-anemometry records realized at several locations under different forcing conditions and analyzed using wavelet analysis. The shape of the excitation signal is fairly well preserved in most of the cases throughout the jet tube, up to the jet exit, as shown in Figs. 13a and 13c. An acoustic resonance observed in the flowmeter time records associated with a Helmholtz volumetric mode is consistently found throughout the tests, regardless of the forcing parameters at $St_\infty = 0.750$. This signature is also observed directly at the jet exit in Figs. 13a and 13c, but not further downstream.

The wavelet analysis of anemometry records in Figs. 13a and 13b confirms the qualitative observations from Mie scattering visualizations, exhibiting signatures of quasi-unforced states at, respectively, $St_\infty = 0.175$ and 0.230, similar to those found in unforced jets at corresponding blowing ratios, i.e., $St_\infty = 0.210$ for BR = 0.438 and $St_\infty = 0.180$ for BR = 0.325, along with their first harmonic and subharmonic. At higher forcing frequencies of $St_\infty = 0.079$ and 0.159, the wavelet decompositions in Figs. 13c and 13d are overwhelmed by the respective forcing-frequency signatures and first harmonics, characteristic of the passage of the starting vortices at the probe location generated only once per cycle. No other significant signature was found on the records, showing the absence of quasi-unforced states.

B. Numerical Results

A series of selected cases was simulated using LES and compared with their experimental equivalents. The low blowing ratio was kept constant at $\mathrm{BR}_l = 0.188$, whereas mean blowing ratio and duty cycle were varied. The three cases presented here correspond to cases 8, 9, and 17 and will be identified using BR_m, duty cycle (DC), and St_∞ only, and the other parameters are available in Table 2. At $\mathrm{BR}_m = 0.350$ and DC = 50% (case 9) for $St_\infty = 0.016$, the behavior of the pulsed jet observed in simulations is very similar to that in the experiments. Figures 14a–14e show a sequence of *X-Z* images from the experiments and their counterparts from the simulations, shaded using temperature levels. The difference in respective diffusivities (mass diffusivity of the TiO_2 particles for the former and thermal diffusivity for the latter) accounts for the differences in the smearing spread of the contours, since the Schmidt number for the particles can be as much as three orders of magnitude larger than the Prandtl number of air. Nevertheless, good qualitative structural agreement was found between experiments and simulations.

The starting vortex formed at the low- to-high blowing-ratio transition is a large hairpin vortex, followed by a series of smaller hairpin vortices in the simulation, as in the experiment, even though the jet is transitional in equivalent unforced conditions at BR= $\mathrm{BR}_h = 0.512$. This behavior is explained in Fig. 15 by the presence of a high-pressure region above the jet exit in the low part of the previous cycle, comparable with that observed in unforced cases (e.g., Fig. 7); at the jet onset, this forces jet fluid to exit on the sides and at the upstream lip beneath the principal horseshoe vortex. This injection creates an early separation of the crossflow boundary layer ahead of the jet exit, and a second horseshoe vortex is formed upstream of the first one, as shown in Figs. 15b–15d.

During the early stages of the BR_l-to-BR_h transient regime, jet fluid continuously flows from the upstream edge of the jet, weakening the inner vortex, while slightly elevating and enhancing the principal horseshoe vortex and therefore temporarily preventing shedding of the inner vortex. Figures 16a–16c show an increase of the cooled area around the jet during the low-to-high transient part of the cycle relative to the previous low-blowing-ratio part. This is confirmed in Fig. 17 by the trends of the time-dependent η_{area} and C_c values over a cycle. An increase in η_{area} and $C_c(\eta < 0.5)$ is observed immediately after the transition from low-to-high blowing ratio over one-quarter of the cycle period ($t^* < 25\%$), compared with the values during the low part of the cycle. The supply of jet fluid to the upstream region is slowly disrupted as the pressure overshoot from the low-to-high blowing-ratio transition settles and the difference in pressure increases across the jet/crossflow interface (Figs. 15b–15d). Gradually, the secondary horseshoe vortex is dissipated, the principal horseshoe vortex decreases in size while moving closer to the wall, and the inner vortex gains in strength. Finally, in Fig. 15d, the inner vortex is free to be transported and the jet behaves in a quasi-unforced manner at BR = 0.512. In Fig. 16d, the coverage is dramatically affected as the jet becomes transitional, which is also observed in Fig. 17 as the values of η_{area} and C_c decrease continuously during the remaining high part of the cycle, therefore partly counterbalancing

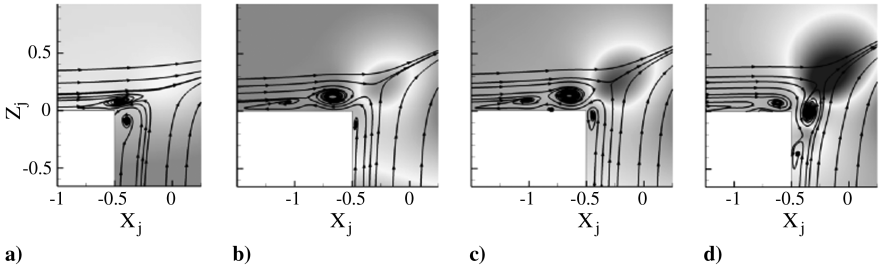

Fig. 15 Two-dimensional streamlines and pressure contours near the jet exit for $\mathbf{BR}_m = 0.35$**, DC = 50% (case 9) and** $St_\infty = 0.016$ **from LES. Time correspond to Fig. 17; a)** $t^* = -3$**, b)** $t^* = 8$**, c)** $t^* = 20$**, and d)** $t^* = 43$**.**

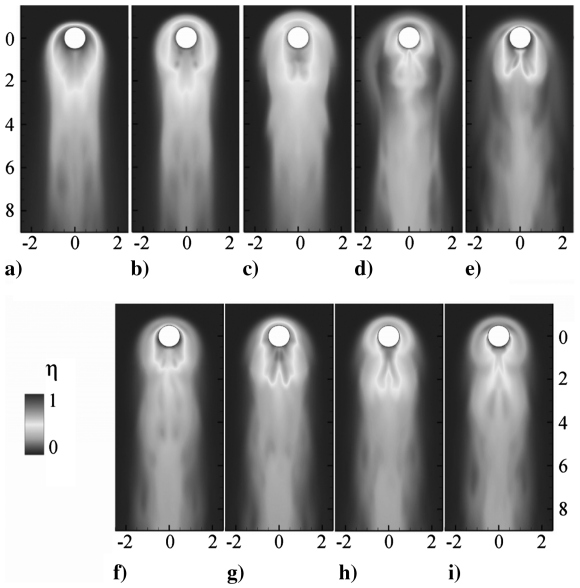

Fig. 16 Instantaneous wall adiabatic effectiveness contours from LES. $BR_m = 0.35$, DC = 50% (case 9) at $St_\infty = 0.016$, with time stamps according to Fig. 17 (top row) and at $St_\infty = 0.159$, with time stamps according to Fig. 21 (bottom row): a) $t^* = -3$, b) $t^* = 8$, c) $t^* = 20$, d) $t^* = 43$, e) $t^* = 60$, f) $t^* = -16$, g) $t^* = 20$, h) $t^* = 44$, and i) $t^* = 72$.

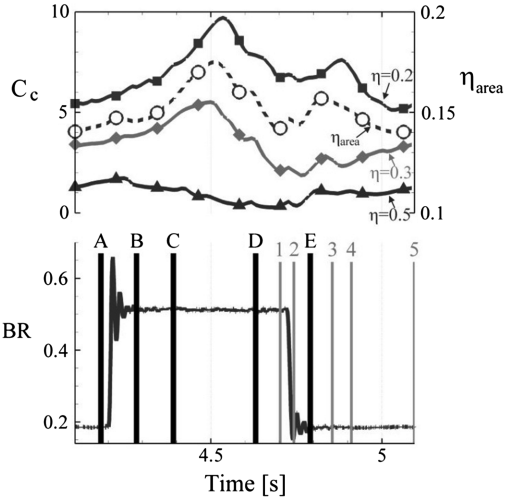

Fig. 17 $BR_m = 0.35$, DC = 50% (case 9) at $St_\infty = 0.016$. Instantaneous coverage coefficient (solid line) and area-averaged adiabatic effectiveness (dashed line) (top) and typical blowing-ratio profile over a cycle (bottom). Vertical bars represent snapshot instants for Figs. 14–16 and 18.

the positive effects of the first part of the cycle. These trends provide some guidance toward tailoring the forcing signal in order to improve film-cooling metrics. Truncating the high part of the cycle, before the quasi-unforced high-blowing-ratio state settles (e.g., for case 9 before $t^* = 25\%$), could prevent the performance degradation after the transient associated with the arrival of the pulse has washed out, while retaining the initial improvement associated with the arrival of the pulse.

The fall of the blowing ratio is accompanied by ingestion of crossflow fluid at the jet upstream lip, evidenced in Fig. 14e and hot crossflow fluid is entrained inside the feeding tube by the inner vortex. As the jet settles in the low-blowing-ratio quasi-unforced state, this pocket of hot fluid is slowly evacuated, though not completely, since it is still visible inside the jet pipe in Fig. 14a (right) only moments before the next pulse. Figures 18a–18e show a time sequence of the flowfield after the valve closing, corresponding to case 9 at $St_\infty = 0.016$. The flow inside the jet pipe separates at both upstream and downstream edges, which leads to multiple rollups of the jet shear layer and significant entrainment of crossflow fluid at the leading edge, therefore partly explaining the lowest performance of the pulsed jet during the BR_h-to-BR_l transient part of the cycle relative to the unforced jet observed in Fig. 17. Eventually, the multiple upstream rollups of the jet shear layer merge (Fig. 18d), and a flow configuration equivalent to the corresponding unforced jet (Fig. 18e) slowly settles in, although the cooling performance is not stabilized until the next pulse, as all three coverage coefficients keep increasing into the next cycle. Given the time stamps of Fig. 17 it appears that under the forcing conditions corresponding to case 9 at $St_\infty = 0.016$, the high-to-low transient regime time scale is only slightly less than 500 ms ($t^* = 50\%$), therefore explaining the strong negative impact on the overall cooling performance. This indicates that a smoother transition from BR_h to BR_l, for instance, via a ramp signal, could suppress part of the ingestion by decreasing the mass deficit induced by the rapid drawdown of the jet.

Figure 19 presents experimental and numerical visualizations for case 9 at a higher forcing frequency of $St_\infty = 0.159$. The qualitative agreement between the experiments and simulations is good, and both exhibit a large starting hairpin vortex. Although the inner vortex is pushed outside the feeding tube in Fig. 19b, the upward

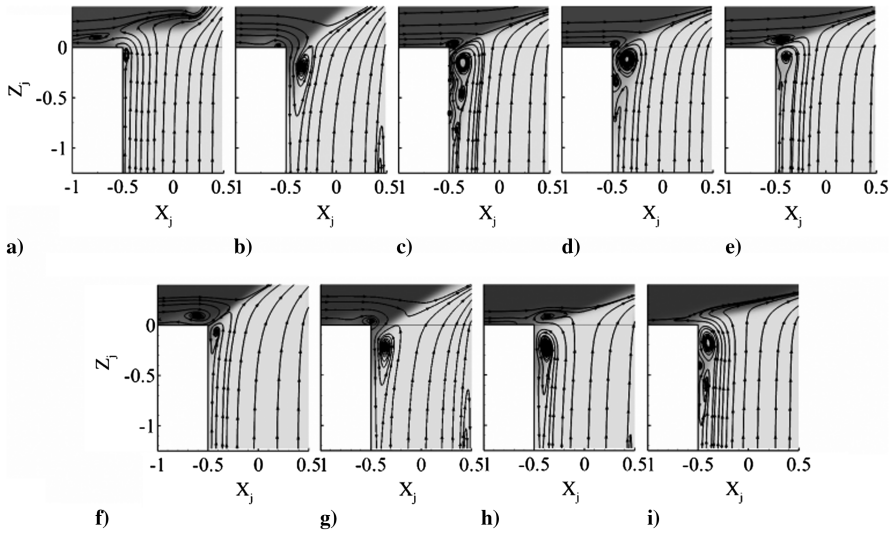

Fig. 18 Ingestion of crossflow fluid at the jet upstream edge from LES of case 9 evidenced by temperature contours and 2-D streamlines. $St_\infty = 0.016$, with time stamps according to Fig. 17 (top) and $St_\infty = 0.159$, with time stamps according to Fig. 21 (bottom): a) $t^* = 50$, b) $t^* = 54$, c) $t^* = 65$, d) $t^* = 70$, e) $t^* = 90$, f) $t^* = -4$, g) $t^* = 44$, h) $t^* = 64$, and i) $t^* = 88$.

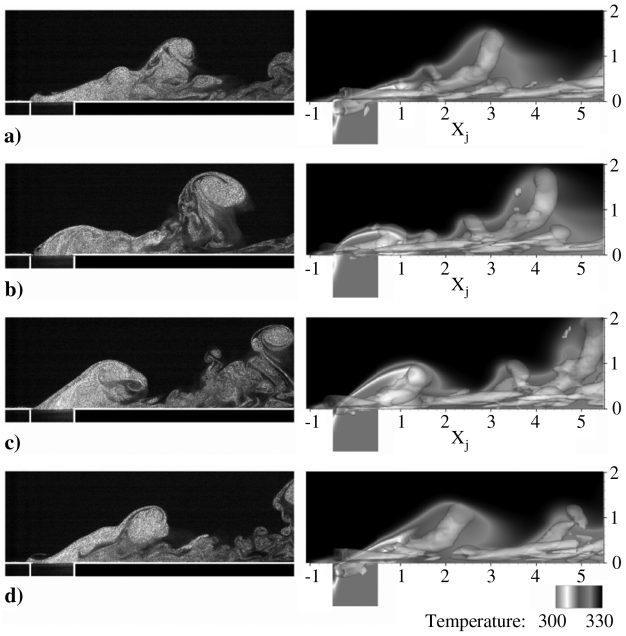

Fig. 19 *X-Z* Mie scattering visualizations from $BR_m = 0.35$, DC = 50% (case 9) at $St_\infty = 0.159$ (left) and *X-Z* Temperature slice from LES and $\Delta P = 3000$ isosurfaces (right). Time stamps according to Fig. 21; a) $t^* = -16$, b) $t^* = 20$, c) $t^* = 44$, and d) $t^* = 72$.

momentum provided by the pulse is not high enough to overcome the high-pressure region above the jet exit; hence, the structure is pushed back in the feeding tube. In Figs. 16f–16i, injection of jet fluid in the upstream region occurs briefly at the jet onset, but is not as prominent as that observed at a lower forcing frequency and is rapidly stopped as the jet draws down. At the transition from BR_h to BR_l, crossflow is ingested inside the jet pipe and triggers the transport of the horseshoe vortex shown in Fig. 19d, disrupting the legs of the structure. A pocket of hotter fluid is formed at the upstream edge of the jet pipe, which will subsist until the next cycle. Figure 20 shows the strong entrainment of crossflow fluid generated by the starting vortex and the early crossflow penetration occurring due to the absence of the horseshoe-vortex legs, also suggested by the narrow instantaneous adiabatic effectiveness contours at $X_j = 1.5$ in Figs. 16f–16i. The time sequence of Figs. 18f–18i reveals flow separation inside the jet pipe at the transition from BR_h to BR_l, as in the corresponding case at a lower forcing frequency, although the extent of the ingestion appears to be lessened by the fact that this transition occurred while the jet was still in the high part of the transient regime at the moment of the jet drawdown, resulting in a smaller pocket of hot fluid inside the jet pipe. It should also be noted that in Fig. 18i several shear-layer rollups are formed, yet not as many as in Fig. 18c, due to insufficient time in the low part of the cycle at $St_\infty = 0.159$, compared with the observed time scales involved at a lower forcing frequency. Most of the coolant is brought to the wall during the low part of the cycle, although in Fig. 21 the instantaneous area-averaged adiabatic

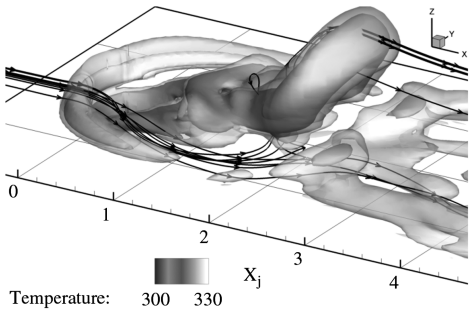

Fig. 20 Stream traces and $\Delta P = 3000$ isosurfaces at $t^* = 72$, shaded with temperature for $BR_m = 0.350$ and DC = 50% (case 9) at $St_\infty = 0.159$ from LES.

effectiveness and coverage coefficient are, surprisingly, almost constant throughout the entire cycle.

Case 8 at $St_\infty = 0.159$ has $BR_m = 0.35$ identical to that of case 9, but a lower duty cycle of 25% (thus, higher BR_h). In Fig. 22a the starting vortex observed in the simulations consists of a highly distorted vortex ring with a prominent downstream part, a slowly convected upstream rollup, and stretched side arms. Because of the high momentum provided by the strong impulse, the downstream rollup moves rapidly away from the wall, while the side arms are reoriented in the vertical direction, thus providing only marginal wall coverage. Because of the short duty cycle, most of the jet fluid in the high part of the cycle is concentrated in the starting structure, while actual wall coverage is provided during the low part of the cycle. According to the classification in Fig. 12 at forcing conditions corresponding to case 8, a complete single starting-vortex ring was expected to be formed instead of a distorted vortex ring, usually observed in the limiting cases at $BR_h \approx 0.584$. This shift in the limiting value of the blowing ratio between starting hairpin and ring vortex was attributed to the same issue causing the shift in transitional blowing ratio for the unforced jets. Case 17 at $St_\infty = 0.159$ has DC identical to that of case 9, but with higher $BR_m = 0.45$ and BR_h. Figure 22b shows the formation of a large starting hairpin vortex with significant crossflow fluid entrainment near the structure. However, compared with case 9, the legs of the starting vortex remain closer to the wall, resulting in better coverage. Additionally, the duty cycle of 50% allows for the formation of trailing hairpin vortices of lower vorticity staying closer to the wall and a longer injection at the upstream edge.

Although the simulations predicted fairly well the formation of starting hairpin vortices for cases 9 and 17, they provided only partial agreement in case 8 with the formation of a distorted ring vortex. These observations are consistent with the inability of the simulations to accurately predict the threshold parameters such as the transitional blowing ratio under unforced conditions or the ring-vortex formation threshold in forced experiments.

Time-averaged values for η_{span}, η_{area}, and C_c were extracted from simulated adiabatic effectiveness and are presented in Fig. 23 and Table 3. Results corresponding to case 9 show that forced jets at $St_\infty = 0.016$ and 0.159 have very comparable performances in terms of spanwise-averaged effectiveness and coverage, despite the significant fluctuations of instantaneous values of η_{span} and C_c observed in Fig. 17 at $St_\infty = 0.016$, compared with quasi-steady values at $St_\infty = 0.159$ in Fig. 21. Overall, these two cases have spanwise-averaged adiabatic effectiveness values approximately 30% lower than the corresponding unforced jet at equivalent mean blowing ratio ($BR = BR_m$). Accordingly, the coverage coefficients of Table 3 are, on average, 50 to 70% lower than corresponding unforced-jet values

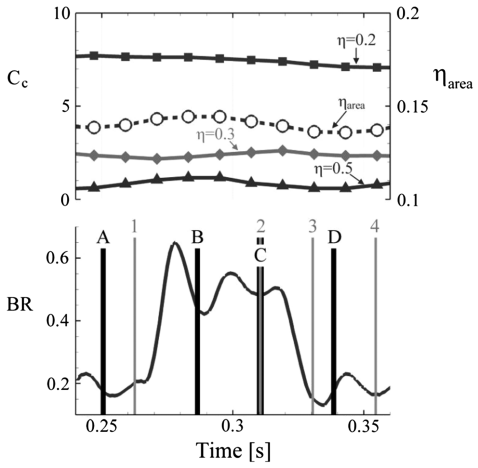

Fig. 21 $BR_m = 0.35$, DC = 50% (case 9) at $St_\infty = 0.159$. Instantaneous coverage coefficient (solid line) and area-averaged adiabatic effectiveness (dashed line) (top) and typical blowing-ratio profile over a cycle. Vertical bars represent snapshot instants for Figs. 15, 17, and 18 (bottom).

at constant mass flow. The area-averaged adiabatic effectiveness is similar.

Simulations for case 8 showed significantly reduced performance compared with equivalent unforced results, with 90 and 65% decreases in C_c and η_{area}, respectively, attributed to the high value of BR_{pp} yielding strong starting vortices carrying coolant away from the wall, while generating large mass deficit at the jet drawdown and considerable crossflow ingestion. The last two simulations at $\text{BR}_m = 0.45$, corresponding to case 17, show some improvement over the corresponding unforced-jet results directly downstream of the jet exit for $X_j < 4$. The coverage coefficients of the forced cases in Table 3 match or exceed the values of the unforced jet when $St_\infty = 0.159$, and the values of η_{area} are comparable with the unforced one.

Overall, the forcing frequency appeared to have only a limited influence on film-cooling performance of the jet for case 9 and case 17. However, flow visualizations have revealed that the degradation of the film-cooling performance at $St_\infty = 0.016$ can be attributed to the settling of the jet in the high part of the cycle with transitional features such as the transport of the inner vortex, while at $St_\infty = 0.159$ the high entrainment of crossflow fluid generated by the starting vortex is responsible for such performance decrease. The same outcome in terms of thermal performance is effectively perpetrated by different flow dynamic mechanisms. In the present study, jet forcing around an average value below the steady-state transitional threshold had a greater influence (yet detrimental) on the film-cooling metrics than does forcing around an average value beyond the transitional threshold. This difference shows that the beneficial effect of decreasing the blowing ratio below the transitional value during the low part of the cycle is less significant than the detrimental action of increasing it above this threshold.

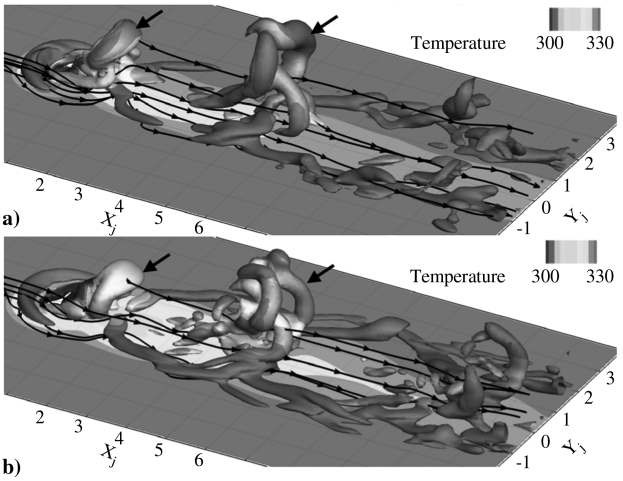

Fig. 22 $\Delta P = 3000$ isosurfaces and stream traces for $St_\infty = 0.159$: a) $\text{BR}_m = 0.350$ and DC = 25% (case 8) and b) $\text{BR}_m = 0.450$ and DC = 50% (case 17) from LES. Arrows indicate consecutive starting vortices.

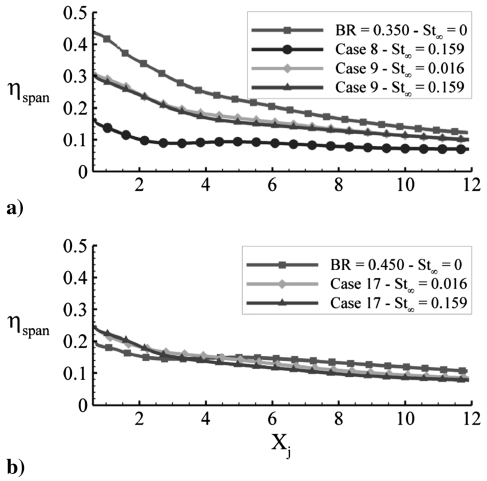

Fig. 23 Spanwise-averaged adiabatic effectiveness for forced jet in crossflow and associated constant-mass-flow-rate unforced jet from LES.

Table 3 Coverage coefficient and area-averaged adiabatic effectiveness from LES under forced conditions, compared with equivalent-mass-flow-rate unforced cases

	C_c			
Conditions	$\eta = 0.2$	$\eta = 0.3$	$\eta = 0.5$	η_{area}
$\text{BR} = \text{BR}_m = 0.350 - St_\infty = 0$	12.82	7.02	2.15	0.226
$\text{BR} = \text{BR}_h = 0.513 - St_\infty = 0$	7.05	1.47	0.21	0.123
Case 9, $St_\infty = 0.016$	7.22	3.23	0.81	0.162
Case 9, $St_\infty = 0.159$	7.26	2.63	0.66	0.145
$\text{BR} = \text{BR}_h = 0.836 - St_\infty = 0$	1.91	0.21	0.05	0.071
Case 8, $St_\infty = 0.159$	1.99	0.75	0.30	0.079
$\text{BR} = \text{BR}_m = 0.450 - St_\infty = 0$	7.25	1.68	0.30	0.122
$\text{BR} = \text{BR}_h = 0.720 - St_\infty = 0$	3.96	0.47	0.08	0.093
Case 17, $St_\infty = 0.016$	5.62	1.91	0.20	0.121
Case 17, $St_\infty = 0.159$	4.29	1.39	0.34	0.113
$\text{BR} = 0.415$, $St_\infty = 0$	14.42	7.87	2.17	0.247

VI. Conclusions

Experimental and numerical work has been conducted on a vertical jet in crossflow under unforced and forced conditions. The baseline unforced-jet study covering low blowing ratios not previously investigated has described the vortical dynamics of both attached and detached regimes, as well as the evolution of the characteristic structures during the transition between them (transitional regime). In the attached regime, the horseshoe vortex was found to have an overall beneficial impact on film spread on the wall by entraining jet coolant upstream of the jet exit and away from the symmetry plane. Above the transitional blowing-ratio threshold, the transport of the inner vortex triggered intermittent disruptions of the horseshoe-vortex system, allowing early crossflow penetration directly downstream of the jet exit and interrupting coolant flow to the upstream regions, which significantly impacted film-cooling performance.

Experimental results for the forced jets showed good qualitative agreement with previous and present numerical simulations in terms of the starting structures generated at the jet onset and their evolution, albeit with some quantitative inconsistencies in the thresholds of transition between the identified structural regimes. Under certain forcing conditions, the transient dynamics introduced at the pulse onset caused a significant increase in coverage by temporarily suppressing the convection of the inner vortex while operating the jet at blowing ratios above the unforced transitional regime threshold. However, this improvement was counterbalanced by subsequent degradation of the performance associated with the quasi-unforced state in the second half of the high part of the cycle. The abrupt decrease in jet flow rate at the transition from high-to-low blowing ratios created a significant mass deficit resulting in internal jet flow separation and ingestion of crossflow fluid inside the jet pipe, strongly affecting film-cooling performance throughout most of the low part of the cycle.

Film-cooling performance of forced jets was compared with unforced cases at fixed mass flow rate and found to be consistently lower in terms of spanwise average adiabatic effectiveness, coverage and area-averaged adiabatic effectiveness with respect to the best performing unforced jet. Considering a transitional regime baseline at $\text{BR} = 0.45$, forcing the jet showed improvement in adiabatic effectiveness and coverage in the vicinity of the jet exit, while area-averaged adiabatic effectiveness was unaffected. Although the duty-cycle effect at constant BR_m was significant, forcing frequencies appeared to have only minor influence on the jet performance, even though they greatly affected the jet flow behavior.

By observing and understanding the dynamics of the characteristic vortical structures formed under pulsed conditions and their impact on the wall-cooling performance, some basis was provided to engineer an optimum forcing signal. In particular, exploiting the improvement observed in the transient part (low-to-high blowing-ratio transition) after the arrival of the pulse, but shortening the high part of the cycle to suppress the quasi-unforced high-blowing-ratio state, could alleviate performance degradation associated with jets in the transitional regime. In addition, a more progressive transition from high-to-low blowing ratios could lessen the extent of crossflow ingestion and the associated film-cooling performance degradation.

Acknowledgments

The authors would like to thank the U.S. Air Force Office of Scientific Research and the associated Program Managers, Lt. Col. Rhett Jefferies and John Schmisseur, for supporting this work under grant FA9550-06-1-0335, as well as the Louisiana Board of Regents for supporting an instrumentation enhancement through grant LEQSF(2006-07)-ENH-TR-14. Computing resources were available through the Louisiana Optical Network Initiative (LONI) at Louisiana State University. The authors would also like to acknowledge the work of Pierre-Emanuel Bouladoux and Jeremiah E. Oertling, who acquired part of the experimental data presented in the current paper.

References

[1] Fric, T. F., and Roshko, A., "Vortical Structure in the Wake of a Transverse Jet," *Journal of Fluid Mechanics*, Vol. 279, 1994, pp. 1–47. doi:10.1017/S0022112094003800

[2] Bunker, R. S., "A Review of Shaped Hole Turbine Film-Cooling Technology," *Journal of Heat Transfer*, Vol. 127, No. 4, 2005, pp. 441–453. doi:10.1115/1.1860562

[3] Nasir, H., Acharya, S., and Ekkad, S., "Improved Film Cooling from Cylindrical Angled Holes with Triangular Tabs: Effect of Tab Orientations," *International Journal of Heat and Fluid Flow*, Vol. 24, No. 5, 2003, pp. 657–668. doi:10.1016/S0142-727X(03)00082-1

[4] Ligrani, P. M., Gong, R., Cuthrell, J. M., and Lee, J. S., "Bulk Flow Pulsations and Film Cooling—I. Injectant Behavior," *International Journal of Heat and Mass Transfer*, Vol. 39, No. 11, 1996, pp. 2271–2282. doi:10.1016/0017-9310(95)00286-3

[5] Bell, C. M., Ligrani, P. M., Hull, W. A., and Norton, C. M., "Film Cooling Subject to Bulk Flow Pulsations: Effects of Blowing Ratio, Freestream Velocity, and Pulsation Frequency," *International Journal of Heat and Mass Transfer*, Vol. 42, No. 23, 1999, pp. 4333–4344. doi:10.1016/S0017-9310(99)00088-5

[6] Narayanan, S., Barooah, P., and Cohen, J. M. "Dynamics and Control of an Isolated Jet in Crossflow," *AIAA Journal*, Vol. 41, No. 12, 2003, pp. 2316–2320. doi:10.2514/2.6847

[7] M'Closkey, R. T., King, J. M., Cortelezzi, L., and Karagozian, A. R., "The Actively Controlled Jet in Crossflow," *Journal of Fluid Mechanics*, Vol. 452, 2002, pp. 325–335. doi:10.1017/S0022112001006589

[8] Coulthard, S. M., Volino, R. J., and Flack, K. A., "Effect of Jet Pulsing on Film Cooling-Part I: Effectiveness and Flow-Field Temperature Results," *Journal of Turbomachinery*, Vol. 129, No. 2, 2007, pp. 232–246. doi:10.1115/1.2437231

[9] Ekkad, S., Ou, S., and Rivir, R. B., "Effect of Jet Pulsation and Duty Cycle on Film Cooling from a Single Jet on a Leading Edge Model," *Journal of Turbomachinery*, Vol. 128, July 2006, pp. 564–571. doi:10.1115/1.2185122

[10] Ou, S., and Rivir, R. B., "Shaped-Hole Film Cooling with Pulsed Secondary Flow," *ASME Turbo Expo*, ASME International, New York 2006.

[11] Womack, K. M., Volino, R. J., and Schultz, M. P., "Combined Effects of Wakes and Jet Pulsing on Film Cooling," *Journal of Turbomachinery*, Vol. 130, No. 4, 2008, pp. 041010. doi:10.1115/1.2812335

[12] Hale, C. A., Plesniak, M. W., and Ramadhyani, S., "Film Cooling Effectiveness for Short Film Cooling Holes Fed by a Narrow Plenum," *Journal of Turbomachinery*, Vol. 122, No. 3, 2000, pp. 553–557. doi:10.1115/1.1303705

[13] Plesniak, M. W., "Noncanonical Short Hole Jets-in-Crossflow for Turbine Film Cooling," *Journal of Applied Mechanics*, Vol. 73, No. 3, 2006, pp. 474–482. doi:10.1115/1.2130359

[14] Burd, S. W., Kaszeta, R. W., and Simon, T. W., "Measurements in Film Cooling Flows: Hole L/D and Turbulence Intensity Effects," *Journal of Turbomachinery*, Vol. 120, No. 4, 1998, pp. 791–798. doi:10.1115/1.2841791

[15] Goldstein, R. J., Eckert, E. R. G., and Burggraf, F., "Effects of Hole Geometry and Density on Three-Dimensional Film Cooling," *International Journal of Heat and Mass Transfer*, Vol. 17, No. 5, 1974, pp. 595–607. doi:10.1016/0017-9310(74)90007-6

[16] Lutum, E., and Johnson, B. V., "Influence of the Hole Length-to-Diameter Ratio on Film Cooling With Cylindrical Holes," *Journal of Turbomachinery*, Vol. 121, No. 2, 1999, pp. 209–216. doi:10.1115/1.2841303

[17] Torrence, C., and Compo, G. P., "A Practical Guide to Wavelet Analysis," *Bulletin of the American Meteorological Society*, Vol. 79, No. 1, 1998, pp. 61–78. doi:10.1175/1520-0477(1998)079<0061:APGTWA>2.0.CO;2

[18] Nikitopoulos, D. E., Oertling, J., Acharya, S., and F. M., "On Active Control of Film-Cooling Flows," *ASME Turbo Expo: Power for Land, Sea and Air*, ASME International, New York, 2006.

[19] Gopalan, S., Abraham, B. M., and Katz, J., "The Structure of a Jet in Cross Flow at Low Velocity Ratios," *Physics of Fluids*, Vol. 16, No. 6, 2004, pp. 2067–2087. doi:10.1063/1.1697397

[20] Kelso, R. M., Lim, T. T., and Perry, A. E., "An Experimental Study of Round Jets in Crossflow," *Journal of Fluid Mechanics*, Vol. 306, 1996, pp. 111–144. doi:10.1017/S0022112096001255

[21] Perry, A. E., and Lim, T. T., "Coherent Structures in Coflowing Jets and Wakes," *Journal of Fluid Mechanics*, Vol. 88, No. 3, 1978, pp. 451–463. doi:10.1017/S0022112078002207

[22] Guo, X., Schröder, W., and Meinke, M., "Large-Eddy Simulations of Film Cooling Flows," *Computers and Fluids*, Vol. 35, No. 6, 2006, pp. 587–606. doi:10.1016/j.compfluid.2005.02.007

[23] Megerian, S., Davitian, J., De B. Alves, L. S., and Karagozian, A. R., "Transverse-Jet Shear-Layer Instabilities. Part 1. Experimental Studies," *Journal of Fluid Mechanics*, Vol. 593, 2007, pp. 93–129. doi:10.1017/S0022112007008385

[24] Jeong, J., and Hussain, F., "On the Identification of a Vortex," *Journal of Fluid Mechanics*, Vol. 285, 1995, pp. 69–94. doi:10.1017/S0022112095000462

[25] Eroglu, A., and Breidenthal, R. E., "Structure, Penetration, and Mixing of Pulsed Jets in Crossflow," *AIAA Journal*, Vol. 39, No. 3, 2001, pp. 417–423. doi:10.2514/2.1351

[26] Johari, H., Pacheco-Tougas, M., and Hermanson, J. C., "Penetration and Mixing of Fully Modulated Turbulent Jets in Crossflow," *AIAA Journal*, Vol. 37, No. 7, 1999, pp. 842–850. doi:10.2514/2.7532

[27] Johari, H., "Scaling of Fully Pulsed Jest in Crossflow," *AIAA Journal*, Vol. 44, No. 11, 2006, pp. 2719–2725. doi:10.2514/1.18929

[28] Sau, R., and Mahesh, K., "Dynamics and Mixing of Vortex Rings in Crossflow," *Journal of Fluid Mechanics*, Vol. 604, 2008, pp. 389–409. doi:10.1017/S0022112008001328

[29] Gharib, M., Rambod, E., and Shariff, K., "A Universal Time Scale for Vortex Ring Formation," *Journal of Fluid Mechanics*, Vol. 360, 1998, pp. 121–140. doi:10.1017/S0022112097008410

L. Cattafesta
Associate Editor